



DETECTING EXOMOONS AROUND SELF-LUMINOUS GIANT EXOPLANETS THROUGH POLARIZATION

SUJAN SENGUPTA¹ AND MARK S. MARLEY²

¹Indian Institute of Astrophysics, Koramangala 2nd Block, Bangalore 560 034, India; sujan@iiap.res.in

²NASA Ames Research Center, MS-245-3, Moffett Field, CA 94035, USA; Mark.S.Marley@NASA.gov

Received 2016 March 8; accepted 2016 April 15; published 2016 June 15

ABSTRACT

Many of the directly imaged self-luminous gas-giant exoplanets have been found to have cloudy atmospheres. Scattering of the emergent thermal radiation from these planets by the dust grains in their atmospheres should locally give rise to significant linear polarization of the emitted radiation. However, the observable disk-averaged polarization should be zero if the planet is spherically symmetric. Rotation-induced oblateness may yield a net non-zero disk-averaged polarization if the planets have sufficiently high spin rotation velocity. On the other hand, when a large natural satellite or exomoon transits a planet with a cloudy atmosphere along the line of sight, the asymmetry induced during the transit should give rise to a net non-zero, time-resolved linear polarization signal. The peak amplitude of such time-dependent polarization may be detectable even for slowly rotating exoplanets. Therefore, we suggest that large exomoons around directly imaged self-luminous exoplanets may be detectable through time-resolved imaging polarimetry. Adopting detailed atmospheric models for several values of effective temperature and surface gravity that are appropriate for self-luminous exoplanets, we present the polarization profiles of these objects in the infrared during the transit phase and estimate the peak amplitude of polarization that occurs during the inner contacts of the transit ingress/egress phase. The peak polarization is predicted to range between 0.1% and 0.3% in the infrared.

Key words: infrared: planetary systems – occultations – planets and satellites: atmospheres – planets and satellites: detection – polarization – scattering

1. INTRODUCTION

Natural satellites orbiting all planets except Mercury and Venus are consequential members of the solar system. The formation of a large variety of satellites with size ranging from 2600 km to a few kilometers is a natural consequence of planet formation. Therefore, it seems likely that the abundance of planetary systems discovered around other stars should also have a significant number of natural satellites or exomoons orbiting the planets. Indeed both theoretical investigations on the formation and properties as well as observational searches for exomoons have already been initiated (for a review see Heller et al. 2014).

Various methods for detecting exomoons have been suggested and almost all of them rely upon photometric light curves of the star during the transit of the planet. For example, barycentric and photocentric Transit Timing Variation (TTV: Sartoretti & Schneider 1999; Szabo et al. 2006) and Transit Duration Variation (TDV: Kipping 2009) rely upon transit photometry. While TTV is more sensitive to wide-orbit moons, TDV is more sensitive to close-orbit moons. The first and to date the only systematic program searching for exomoons with *Kepler* (the Hunt for Exomoons with *Kepler* program) analyzes the transit light curves obtained by the *Kepler* space telescope and attempts to identify the presence of a natural satellite around the transiting planets (Kipping et al. 2012). Unfortunately, the effect of an exomoon on the light curve is so tiny that the expected signature is extremely difficult to identify, and therefore evidence for an exomoon is still elusive.

Apart from transiting planets, another class of giant exoplanets that are young, warm and self-luminous have been discovered by direct imaging (e.g., Chauvin et al. 2004; Marois et al. 2008; Lafrenière et al. 2010; Lagrange et al. 2010; Macintosh et al. 2015). These planets are typically 10–40 AU

away from their parent stars. Such a large separation allows them to be spatially resolved with coronagraphic observation as well as differential imaging techniques. In the next few years, ground-based telescopes with dedicated high-contrast imaging instrumentation, such as the P1640 coronagraph on Palomar, the Gemini Planet Imager on Gemini South, SPHERE on the VLT, and the *James Webb Space Telescope* are expected to detect many more such planets (Beichman et al. 2010). On the other hand, methods for detecting exomoons around directly imaged exoplanets have been suggested by a few authors (Cabrera & Schneider 2007; Heller & Simon 2014; Heller 2016).

Comparison of synthetic spectra with observed data clearly implies that most of the exoplanets directly imaged to date have dusty atmospheres (Marois et al. 2008; Lafrenière et al. 2010; Macintosh et al. 2015). In that respect the atmospheres of these planets are very similar to those of L dwarfs. Hence, like the L dwarfs, it is expected that radiation from these planets, as well as from those likely to be detected in the future, should be linearly polarized in the near-infrared due to scattering by dust grains (Marley & Sengupta 2011). For a homogeneous distribution of scatterers, the net polarization integrated over the projected disk of a spherically symmetric planet is zero. Horizontal inhomogeneity may yield net non-zero polarization (de Kok et al. 2011). On the other hand, rotation-induced oblateness causes asymmetry and gives rise to a significant amount of polarization (Sengupta & Krishan 2001; Sengupta & Marley 2010; Marley & Sengupta 2011). The observed linear polarization of L dwarfs shows that the amount of polarization increases with increasing spin rotation velocity (Miles-Paez et al. 2013). This implies that the asymmetry due to oblateness plays a dominant role. Apart from the asymmetry due to oblateness, net non-zero disk-integrated polarization may arise

if the stellar disk is occulted by a planet. Several authors have presented detailed models of such transit polarization of stars of different spectral types (Carciofi & Magalhaes 2005; Kostogryz et al. 2011, 2015; Wiktorowicz & Laughlin 2014; Kostogryz & Berdyugina 2015). Scattering of light in stellar atmosphere gives rise to linear polarization throughout the stellar spectrum. Because of the variation in scattering geometry this polarization increases monotonically from the center of the disk toward the stellar limb. However, since the polarization of hot stars arises because of electron scattering and that of cool stars arises because of Rayleigh scattering of atoms and molecules, the peak amplitude of polarization is extremely small, a few times 10^{-6} in the B-band. On the other hand, as demonstrated by Sengupta & Marley (2010) and Marley & Sengupta (2011), scattering by dust grains yields high polarization in the infrared. In fact the degree of polarization detected from several L dwarfs is as high as 0.1%–0.4% in the I-band for even moderately fast rotating L dwarfs.

In this paper, we suggest that, similar to the polarization of a star that arises due to the transit of a planet, self-luminous directly imaged exoplanets should also give rise to detectable amounts of time-dependent polarization if the object is eclipsed by a sufficiently large natural satellite or exomoon. Hence, we propose that exomoons around self-luminous directly imaged planets can be detected through time-dependent image polarimetric observation.

In the next section, we briefly describe the atmospheric models adopted. We present the formalism used to derive the time-dependent eclipse polarization by exomoons of different size in Section 3, and we discuss the results in Section 4. Finally we conclude our investigation in Section 5.

2. THE PLANETARY ATMOSPHERIC MODELS AND SCATTERING POLARIZATION

In order to calculate the intensity and polarization of the planetary radiation, we have employed a grid of one-dimensional, hydrostatic, non-gray atmospheric models in radiative–convective equilibrium and stratified in a plane-parallel geometry. These models incorporate about 2200 gas species, about 1700 solids and liquids for compounds of 83 naturally occurring elements as well as five major condensates as sources of opacity (Ackerman & Marley 2001; Marley et al. 2002; Freedman et al. 2008; Saumon & Marley 2008). Silicate and iron clouds computed with sedimentation efficiency $f_{\text{sed}} = 2$ are included in the atmospheric model (Ackerman & Marley 2001). The model atmospheres are calculated for specified values of effective temperature T_{eff} and surface gravity g .

The atmospheric code computes the temperature–pressure profile, the gas and dust opacity, and the dust scattering asymmetry function averaged over each atmospheric pressure level. These input data are used in a multiple scattering polarization code that solves the radiative transfer equations in vector form. The two Stokes parameter I and Q are calculated in a locally plane-parallel medium (Sengupta & Marley 2010; Marley & Sengupta 2011). A combined Henyey–Greenstein–Rayleigh phase matrix (Liu & Weng 2006) is used to calculate the angular distribution of the photons before and after scattering. The detailed formalisms as well as the numerical methods for calculating the angle-dependent total and polarized intensities I and Q are described in Sengupta & Marley (2009). Finally, the angle-dependent I and the polarization $P = Q/I$ computed by the polarization code are integrated over the

eclipsed disk of the planet. The formalism is described in the next section. We have neglected thermal and reflected light from the exomoon.

3. ECLIPSED DISK-INTEGRATED POLARIZATION

Similar to the case of a transiting planet, the net polarization during eclipse is equal to the fractional circumference blocked by the projection of the moon over the surface of the planet multiplied by the scattering polarization and intensity of the planet at each radial point along the planetary disk.

The disk-integrated polarization during the eclipse phase is given by (Carciofi & Magalhaes 2005; Wiktorowicz & Laughlin 2014)

$$P_{(t)} = \frac{1}{F} \int_{r_m(t)-w}^{r_m(t)+w} C(r, t) I(r) P(r) dr, \quad (1)$$

where F is the flux of the unobscured planet, $I(r)$ and $P(r)$ are the specific intensity and polarization respectively at the normalized radial coordinate r on the disk of the planet, $w = R_m/R_p$ is the ratio between the radius of the moon (R_m) and the radius of the planet (R_p), $C(r, t)$ is the instantaneous path length along the planetary circumference at r that is eclipsed by the moon and is given as

$$C(r, t) = 2\sqrt{[r - r_m(t)]^2 - w^2}, \quad (2)$$

$r_m(t)$ being the instantaneous position of the center of the moon given by

$$r_m(t) = \left[b^2 + 4\{(1+w)^2 - b^2\} \left(\frac{t}{\tau}\right)^2 \right]^{1/2}, \quad (3)$$

where $b = a \cos i/R_p$ is the impact parameter for a circular orbit of radius a and i is the orbital inclination angle of the moon. In the above expression, t is the time since mid-eclipse and τ is the eclipse duration given by (Scharf 2009)

$$\tau = \frac{P}{\pi} \sin^{-1} \left[\frac{R_p}{a} \left\{ \frac{(1+w)^2 - b^2}{1 - \cos^2 i} \right\}^{1/2} \right]. \quad (4)$$

Here, $\mu = \cos \theta$ with θ being the angle between the normal to the planetary surface and the line of sight, $r = \sqrt{1 - \mu^2}$, $0 \leq r \leq 1$. In terms of μ , Equation (1) therefore reduces to

$$P_{(t)} = \frac{1}{F} \int_{r_1}^{r_2} 2 \sqrt{\frac{[(1 - \mu^2)^{1/2} - r_m(t)]^2 - w^2}{1 - \mu^2}} \times I(\mu) P(\mu) \mu d\mu, \quad (5)$$

where $r_1 = \sqrt{1 - [r_m(t) + w]^2}$ and $r_2 = \sqrt{1 - [r_m(t) - w]^2}$.

Similar to the orbital period of Ganymede around Jupiter, we have fixed the orbital period of the exomoon at 7 days and have calculated the orbital distance by using Kepler’s law. The radius of the planet is fixed at $1R_J$ where R_J is the radius of Jupiter. The mass of the planet is calculated from its surface gravity. It is worth mentioning that this is just a representative case. The orbital period does not alter the amount of polarization originating from the eclipse but it determines the interval between two successive amplitudes of polarization that occur at the inner contact points of the transit ingress/egress phase and provides some qualitative guidance on the order of magnitude of the duration of the polarization event. The

polarization profile is calculated for two values of the inclination angle for the satellite, 90° and 88° . Similar to the case of transiting planets, eclipse cannot occur if the inclination angle $i \leq \cos^{-1} \left(\frac{R_p + R_m}{a} \right)$.

4. RESULTS AND DISCUSSION

For transit polarization models of stars, the local angle-dependent polarization arises from scattering of light by atoms and molecules, and the maximum amount of polarization that occurs at the stellar limb is usually very small. Scattering polarization at different angular or radial points of a solar-type star varies from a few times 10^{-4} near the limb to a few times 10^{-6} near the center for wavelengths in the range 4000–5500 Å (Fluri & Stenflo 1999). At longer wavelengths the polarization is much smaller than 10^{-6} . The polarization is of course zero at the center ($\mu = 1$) and maximum at the limb ($\mu = 0$). The contribution of a scattering opacity to the total opacity in the atmosphere is responsible for the center-to-limb variation in the polarization across any stellar disk (Harrington 1969). Electron scattering gives rise to such opacity in hot stars (spectral type O, B, or A), while Rayleigh scattering by atomic and molecular hydrogen and atomic helium is the main source of scattering opacity in cool stars. The polarization at the limb due to electron scattering is as high as 0.1 (Chandrasekhar 1960) while the polarization for wavelengths of solar resonant lines such as Ca or Sr is about 0.16 (Bianda et al. 1999). This is about three orders of magnitude higher than the polarization at the solar limb observed in the solar continuum (Fluri & Stenflo 1999). On the other hand, if the planetary radiation is polarized by dust scattering then the amount of polarization at the limb for the far optical and infrared wavelengths should be higher than that arising from electron scattering at near optical wavelengths. As realized by Carciofi & Magalhaes (2005), formation of dust grains in the cloudy atmosphere of L brown dwarfs would provide an additional scattering opacity to the gas opacity, which should yield into large values for limb polarization. Such a realization prompted Sengupta (2016) to suggest that Earth-size rocky exoplanets transiting cloudy L dwarfs might be detected through time-resolved imaging polarimetry. Self-luminous giant exoplanets are also expected to have a cloudy atmosphere, and linear polarization as large as 1%–2% in the infrared is already predicted by Marley & Sengupta (2011).

In order to check the validity of the formalism adopted and the correctness of the numerical calculations, we reproduced the transit polarization profiles presented by Carciofi & Magalhaes (2005). These authors used the analytical expression for the limb darkening law suggested by Claret (2000) and that for the solar continuum polarization suggested by Fluri & Stenflo (1999). Carciofi & Magalhaes (2005) also estimated the maximum transit polarization of a T dwarf of radius $0.2 R_\odot$ occulted by an Earth-size exoplanet. For $R_m/R_p = 0.046$, Carciofi & Magalhaes (2005) found that the peak amplitude of transit polarization at wavelength 4600 Å is 1.6×10^{-4} or 0.016%. As presented in Figure 1, for the same value of R_m/R_p and for a central eclipse ($i = 90^\circ$), we find the peak polarization to be 0.02% in the B-band, in good agreement with the result of Carciofi & Magalhaes (2005). Figure 1 presents the eclipse polarization profiles in the B-, I-, J-, and H-bands of a self-luminous cloudy exoplanet of radius $1R_J$. In the B-band, Rayleigh scattering by molecules dominates over dust

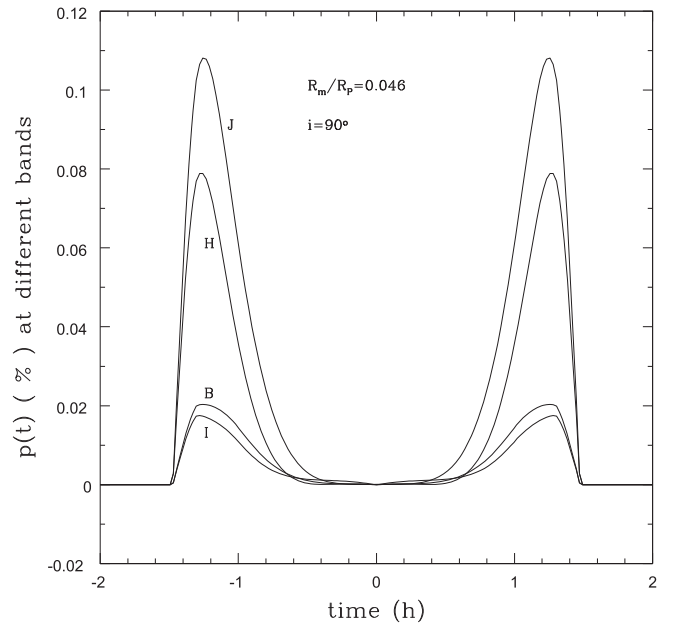


Figure 1. Disk-integrated linear polarization in different wavelength bands of a self-luminous spherical exoplanet partially eclipsed by a moon of radius 0.046 times the radius of the planet. The effective temperature and the surface gravity of the exoplanet are 1000K and 30 ms^{-2} , respectively.

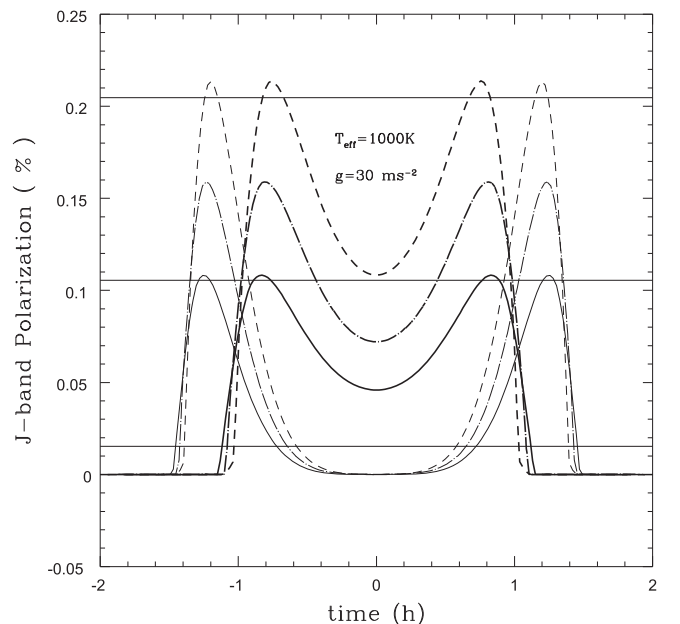


Figure 2. J-band disk-integrated polarization of self-luminous, spherical exoplanets partially eclipsed by an exomoon. Thin and thick lines represent the percentage polarization for an exomoon transit with an orbital inclination angle of $i = 90^\circ$ and 88° respectively. Solid lines, dashed-dotted lines, and dashed lines represent the eclipse polarization profile with $R_m/R_p = 0.046$, 0.07, and 0.1 respectively. The orbital period of the exomoon is set to 7 days for all cases. From top to bottom, the horizontal lines represent linear polarization integrated over the disk of a rotation-induced oblate exoplanet (with no eclipse) with spin period 6.1, 6.6, and 15 hr.

scattering. As the wavelength increases, dust scattering becomes more important in determining the amount of polarization. Figure 1 shows that the eclipse polarization profiles for B- and I-bands are almost the same but the peak polarization increases by about a factor of six in the J-band.

That the polarization in the J-band is much higher than the polarization in the I-band has already been demonstrated by Marley & Sengupta (2011) for a variety of atmospheric and cloud models. The polarization, however, decreases in the H-band as the wavelength of the radiation increases further. The wavelength dependence of the polarization is governed by the adopted cloud model, e.g., the size distribution, the number density of the dust grains, as well as the location of the cloud base and deck.

The disk-integrated polarization of a spherical exoplanet eclipsed by an exomoon is presented in Figure 2 for two different values of the orbital inclination angles and three different sizes of the exomoon. The disk-integrated polarization of an unobscured oblate planet is also presented for comparison. The disk-integrated polarization of a rotation-induced non-spherical and eclipsed planet could be complicated owing to the fact that the net polarization depends on the angle between the spin axis of the planet and the orbital plane of the exomoon. Since it is not possible to determine the orientation of the spin axis of the exoplanet, we restrict our polarization models to slowly rotating eclipsing planets for which the departure from sphericity is too small to yield net non-zero polarization when it is not in eclipsing phase. The projected spin angular velocity of a few self-luminous exoplanets has already been derived from observations (Marois et al. 2010; Snellen et al. 2014) and can provide the minimum value of the oblateness of the object. Disk-integrated polarization for oblate self-luminous giant exoplanets has been presented by Marley & Sengupta (2011) for various values of the spin period, surface gravity, and effective temperature. We have neglected any inhomogeneous distribution of scatterers. Our atmospheric models consider vertically inhomogeneous but horizontally homogeneous cloud distributions.

As shown in Figure 2, the qualitative feature of the eclipse polarization profile is the same as that of transit polarization presented by Carciofi & Magalhaes (2005) and Kostogryz et al. (2011, 2015). The double-peaked polarization profile arises because of the fact that the maximum polarization occurs near the inner contacts of ingress/egress phases. For central eclipse, i.e., when the inclination angle $i = 90^\circ$, the projected position of the center of the moon during mid-eclipse is at the center of the planet, creating a symmetry on the projected stellar disk. Hence the disk-integrated polarization for central eclipse is zero during mid-eclipse. The polarization increases as the moon moves from the center ($t=0$) to the limb ($t = \pm\tau/2$) of the planetary disk because it induces asymmetry on the planetary disk. However, when the eclipse is off-center, i.e., $i < 90^\circ$, the polarization is non-zero during the whole eclipse epoch. The net polarization at mid-eclipse increases with decreasing orbital inclination angle of the moon. However, the peak polarization at the limb remains the same irrespective of the inclination angle. Therefore, the peak polarization is independent of the orbital inclination but depends on the ratio of the radii of satellite and planet. The transit duration depends on the size of both the moon and the planet, on the orbital distance of the moon from the planet, and on the inclination angle. Therefore, for a given orbital distance, the peak polarization occurs at different times for different size ratios and inclination angles. Figure 2 shows that the peak polarization at the inner contacts of the ingress/egress phase increases linearly with increasing size of the exomoon. In the J-band the maximum degree of linear polarization for $R_m/R_p = 0.046$ is 0.11% while that for

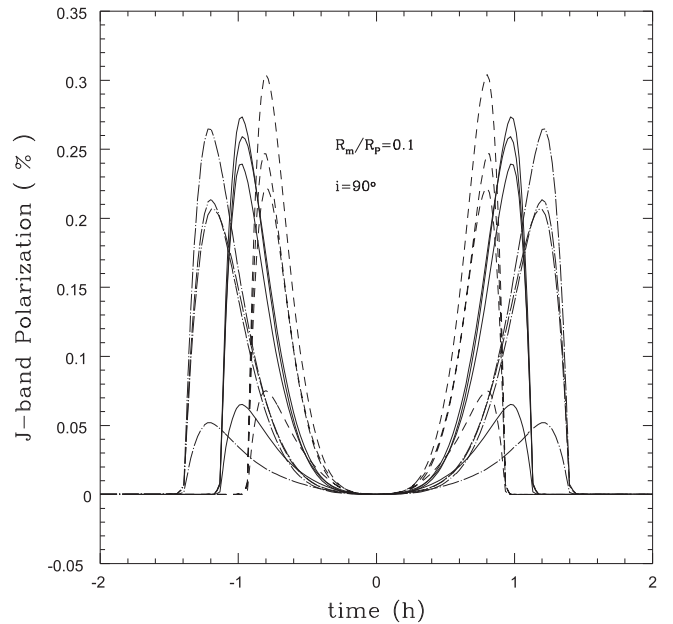


Figure 3. J-band polarization of exoplanets with different effective temperatures and surface gravities. Solid lines represent exoplanet models with $g = 56 \text{ m s}^{-2}$, and with $T_{\text{eff}} = 1000, 1200, 800,$ and 600 K from top to bottom. Dashed lines represent the polarization with $g = 100 \text{ m s}^{-2}$, and with $T_{\text{eff}} = 1200, 1000, 800$ and 600 K from top to bottom. Similarly, dotted-dashed lines represent exoplanet models with $g = 30 \text{ m s}^{-2}$, and with $T_{\text{eff}} = 800, 1000, 1200$ and 600 K from top to bottom.

$R_m/R_p = 0.07$ and 0.1 is 0.16% and 0.21% , respectively. In the absence of an eclipsing exomoon, 0.1% linear polarization can arise only if the spin rotation period of the planet with surface gravity $g = 30 \text{ m s}^{-2}$ is less than 6.6 hr while it needs a spin rotation period less than 6.1 hr to yield a net non-zero disk-integrated polarization of 0.2% . For higher surface gravity, an even shorter period is required in order to yield sufficient oblateness to the planet. Therefore, the time-dependent eclipse polarization can be distinguished from the disk-integrated polarization of an oblate planet if the spin rotation period of the planet is higher than $10\text{--}15 \text{ hr}$, so that the asymmetry due to spin rotation is negligible.

Marley & Sengupta (2011) and Sengupta & Marley (2010) have demonstrated that the degree of polarization of cloudy self-luminous exoplanets and L dwarfs depends on the effective temperature and the surface gravity of the objects. In Figure 3, we present the eclipse polarization profiles for exoplanets with different effective temperatures and surface gravities. At the lowest surface gravity $g = 30 \text{ m s}^{-2}$ among the three cases we consider, the highest polarization is obtained in the J-band when $T_{\text{eff}} = 800 \text{ K}$. If the temperature increases further, the cloud base shifts upward, yielding a smaller column of dust grains in the observed atmosphere, and hence the polarization decreases with increasing effective temperature. A balance between the downward transport by sedimentation and upward turbulent diffusion of condensates and gas determines the scattering opacity and hence the polarization for different effective temperatures and surface gravities. For $g = 56 \text{ m s}^{-2}$, the polarization is maximum at $T_{\text{eff}} = 1000 \text{ K}$ and it decreases with both increasing and decreasing effective temperature. In fact Figure 3 does not show much difference in polarization for $T_{\text{eff}} = 1200$ and 1000 K . On the other hand, at the highest surface gravity considered here, $g = 100 \text{ m s}^{-2}$, the

polarization is greatest at $T_{\text{eff}} = 1200$ K but decreases at lower effective temperatures. Therefore, a combination of the surface gravity and effective temperature along with the size of the exomoon relative to the exoplanet determines the amount of polarization caused by the eclipse. However, the difference in the amount of polarization among these cases is likely too small to be differentiated observationally. Moreover, the effect of surface gravity and effective temperature can be realized even without the eclipsing effect. For example, a sufficiently fast rotator that may yield a detectable amount of net non-zero polarization would show a polarization profile with the same properties. Finally, as seen from Figure 3, if T_{eff} is as low as 600 K then, for any surface gravity, the polarization reduces substantially owing to there being fewer dust grains in the atmosphere probed in the near-infrared in these models. It is worth mentioning that the orbital separation or the inclination angle does not alter the peak amplitude of polarization but alters the overall polarization profile.

5. CONCLUSIONS

We suggest that time-resolved imaging polarimetry may be a potential technique to detect large exomoons around directly imaged self-luminous exoplanets. The cloudy atmosphere of such planets would ensure high polarization due to scattering by dust grains. However, the disk-integrated net polarization would be zero if the planet is spherically symmetric. This symmetry is broken either if the planet loses sphericity due to fast spin rotation, if it has horizontally inhomogeneous cloud structures, or if a sufficiently large satellite eclipses the planetary surface. Asymmetry due to a combination of the above causes is also possible. Assuming a spherical exoplanet eclipsed by an exomoon, we estimated the peak polarization at the inner contact points of the ingress/egress phase and presented the eclipse polarization profile. Our investigation implies that a detectable amount of polarization may arise in the J-band if the planet is eclipsed by a large exomoon. For a central eclipse, the detectable amount of polarization would arise only at the inner contacts of the ingress/egress phase, while for an off-central eclipse, polarization may be detectable during the entire eclipsing phase. Unlike the constant polarization that may be detected for a fast rotating exoplanet, no polarization will be detected when the planet is out of the eclipse phase.

According to our estimation, an image polarimeter with sensitivity ranging from 0.3% to 0.01% may detect the presence of exomoon around the self-luminous exoplanets that are directly imaged. Future high-contrast imaging instruments

on telescopes of 30 m class may plausibly provide both the time resolution and polarimetric sensitivity to detect such moons.

We thank the reviewer for a critical reading of the manuscript and for providing several useful suggestions.

REFERENCES

- Ackerman, A., & Marley, M. S. 2001, *ApJ*, **556**, 872
 Beichman, C. A., Krist, J., Trauger, T., et al. 2010, *PASP*, **122**, 162
 Bianda, M., Stenflo, J. O., & Solanki, S. K. 1999, *A&A*, **350**, 1060
 Cabrera, J., & Schneider, J. 2007, *A&A*, **464**, 1133
 Carciofi, A. C., & Magalhaes, A. M. 2005, *ApJ*, **635**, 570
 Chandrasekhar, S. 1960, *Radiative Transfer* (New York: Dover)
 Chauvin, G., Lagrange, A.-M., Dumas, C., et al. 2004, *A&A*, **425**, L29
 Claret, A. 2000, *A&A*, **363**, 1081
 de Kok, R. J., Stam, D. M., & Karalidi, T. 2011, *ApJ*, **741**, 59
 Fluri, D. M., & Stenflo, J. O. 1999, *A&A*, **341**, 902
 Freedman, W. L., Madore, B. F., Rigby, J., Persson, S. E., & Sturch, L. 2008, *ApJS*, **679**, 71
 Harrington, J. P. 1969, *ApL*, **3**, 165
 Heller, R., & Simon, A. 2014, *ApJ*, **796**, L1
 Heller, R. 2016, *A&A*, **588**, 34
 Heller, R., Williams, D., Kipping, D., et al. 2014, *AsBio*, **14**, 798
 Kipping, D. M. 2009, *MNRAS*, **392**, 181
 Kipping, D. M., Bakos, G. A., Buchhave, L., Nesvorný, D., & Schmitt, A. 2012, *ApJ*, **750**, 115
 Kostogryz, N. M., & Berdyugina, S. V. 2015, *A&A*, **575**, 89
 Kostogryz, N. M., Yakobchuk, T. M., & Berdyugina, S. V. 2015, *ApJ*, **806**, 97
 Kostogryz, N. M., Yakobchuk, T. M., Morozhenko, O. V., & VidMachenko, A. P. 2011, *MNRAS*, **415**, 695
 Lafrenière, D., Jayawardhana, R., & van Kerkwijk, M. H. 2010, *ApJ*, **719**, 497
 Lagrange, A.-M., Bonnefoy, M., Chauvin, G., et al. 2010, *Sci*, **329**, 57
 Liu, Q., & Weng, F. 2006, *ApOpt*, **45**, 7475
 Macintosh, B., Graham, J. R., Barman, T., et al. 2015, *Sci*, **350**, 64
 Marley, M. S., & Sengupta, S. 2011, *MNRAS*, **417**, 2874
 Marley, M. S., Seager, S., Saumon, D., et al. 2002, *ApJ*, **568**, 335
 Marois, C., Macintosh, B., Barman, T., et al. 2008, *Sci*, **322**, 5906
 Marois, C., Zuckerman, B., Konopacky, Q. M., Macintosh, B., & Barman, T. 2010, *Natur*, **468**, 1080
 Miles-Paez, P. A., Zapatero Osorio, M. R., Pallé, E., & Peña Ramírez, K. 2013, *A&A*, **556**, 125
 Sartoretti, P., & Schneider, J. 1999, *A&AS*, **134**, 553
 Saumon, D., & Marley, M. S. 2008, *ApJ*, **689**, 1327
 Scharf, C. A. 2009, *Extrasolar Planets and Astrobiology* (Sausalito, CA: Univ. Science Books) Chapter 9
 Sengupta, S. 2016, (arXiv:1604.08701)
 Sengupta, S., & Krishan, V. 2001, *ApJL*, **561**, L123
 Sengupta, S., & Marley, M. S. 2009, *ApJ*, **707**, 716
 Sengupta, S., & Marley, M. S. 2010, *ApJL*, **722**, L142
 Snellen, I. A. G., Brandl, B. R., de Kok, R. J., et al. 2014, *Natur*, **509**, 63
 Szabo, G. M., Sztatmáry, K., Divéki, Z., & Simon, A. 2006, *A&A*, **450**, 395
 Wiktorowicz, S. J., & Laughlin, G. P. 2014, *ApJ*, **795**, 12